

1 **Inter-annual surface evolution of an Antarctic blue-ice moraine** 2 **using multi-temporal DEMs**

3
4 **M. J. Westoby¹, S. A. Dunning², J. Woodward¹, A. S. Hein³, S. M. Marrero³, K. Winter¹**
5 **and D. E. Sugden³**

6
7 [1]{Department of Geography, Engineering and Environment, Northumbria University,
8 Newcastle upon Tyne, UK}

9
10 [2]{School of Geography, Politics and Sociology, Newcastle University, Newcastle upon
11 Tyne, UK}

12
13 [3]{School of GeoSciences, University of Edinburgh, Edinburgh, UK}

14
15 Correspondence to: M. J. Westoby (matt.westoby@northumbria.ac.uk)

16 17 **Abstract**

18
19 Multi-temporal and fine resolution topographic data products are being increasingly
20 used to quantify surface elevation change in glacial environments. In this study, we
21 employ 3D digital elevation model (DEM) differencing to quantify the topographic
22 evolution of a blue-ice moraine complex in front of Patriot Hills, Heritage Range,
23 Antarctica. Terrestrial laser scanning (TLS) was used to acquire multiple topographic
24 datasets of the moraine surface at the beginning and end of the austral summer
25 season in 2012/2013 and during a resurvey field campaign in 2014. A
26 complementary topographic dataset was acquired at the end of season 1 through the
27 application of Structure-from-Motion (SfM) photogrammetry to a set of aerial
28 photographs taken from an unmanned aerial vehicle (UAV). Three-dimensional
29 cloud-to-cloud differencing was undertaken using the Multiscale Model to Model
30 Cloud Comparison (M3C2) algorithm. DEM differencing revealed net uplift and
31 lateral movement of the moraine crests within season 1 (mean uplift ~0.10 m), with
32 lowering of a similar magnitude in some inter-moraine depressions and close to the
33 current ice margin. Our results indicate net uplift across the site between seasons 1
34 and 2 (mean 0.07 m). This research demonstrates that it is possible to detect
35 dynamic surface topographical change across glacial moraines over short (annual to
36 intra-annual) timescales through the acquisition and differencing of fine-resolution
37 topographic datasets. Such data offer new opportunities to understand the process
38 linkages between surface ablation, ice flow, and debris supply within moraine ice.

39 1. Introduction

40

41 Fine-resolution topographic data products are now routinely used for the
42 geomorphometric characterisation of Earth surface landforms (e.g. Passalacqua et
43 al., 2014, 2015; Tarolli, 2014). Recent decades have seen the advent and uptake of
44 a range of surveying technologies for characterising the form and evolution of Earth
45 surface topography at the macro- (landscape; kilometres), meso- (landform; metres)
46 and micro-scales (patch-scale; centimetre-millimetre). These technologies have
47 included, amongst others, the use of satellite remote sensing techniques (e.g. Kääb,
48 2002; Smith et al., 2006; Farr et al., 2007; Stumpf, 2014; Noh and Howat, 2015), as
49 well as field-based surveying platforms such as electronic distance meters (total
50 station; e.g. Keim et al., 1999; Fuller et al., 2003), differential global positioning
51 systems (dGPS; e.g. Brasington et al., 2000; Wheaton et al., 2010), terrestrial laser
52 scanning (TLS; e.g. Rosser et al., 2005; Hodge et al., 2009), airborne light detection
53 and ranging (LiDAR; e.g. Bollmann et al., 2011) and softcopy or digital
54 photogrammetry (e.g. Micheletti et al., 2015).

55

56 More recently, geoscientists are increasingly adopting low-cost Structure-from-
57 Motion with multi-view stereo (SfM-MVS) methods, which employ computer vision
58 and multi-view photogrammetry techniques to recover surface topography using
59 optical (e.g. James and Robson, 2012; Westoby et al., 2012; Javernick et al., 2014;
60 Micheletti et al., 2014; Woodget et al., 2015; Smith and Vericat, 2015) or thermal
61 imagery (e.g. Lewis et al., 2015). Concomitant developments in lightweight
62 unmanned aerial vehicle (UAV) technology, specifically decreasing system costs,
63 increased portability, and improvements in the accessibility of flight planning
64 software have encouraged the acquisition of repeat, fine-resolution (metre to
65 centimetre) topographic data products from low-altitude aerial photography platforms
66 (e.g. Niethammer et al., 2010; Ouédraogo et al., 2014; Bhardwaj et al., 2016).
67 Furthermore, the differencing of topographic datasets acquired at different times is
68 now an established method for quantifying the transfer of mass and energy through
69 landscapes at the spatial scales of observation at which many processes operate
70 (Passalacqua et al., 2015).

71

72 To date, fine-resolution topographic datasets produced using airborne or ground-
73 based light detection and ranging (LiDAR), or terrestrial or low-altitude aerial digital
74 photogrammetry have been used for a diverse range of applications in various
75 glacial, proglacial, and periglacial environments at a range of scales, including: the
76 quantification of ice surface evolution (e.g. Baltsavias et al., 2001; Pitkänen and
77 Kajuutti, 2004; Keutterling and Thomas, 2006; Schwalbe and Maas, 2009;

78 Immerzeel et al., 2014; Pepin et al., 2014; Whitehead et al., 2014; Gabbud et al.,
79 2015; Kraaijenbrink et al., 2015; Piermattei et al., 2015; Ryan et al., 2015); mapping
80 the redistribution of proglacial sediment (e.g. Milan et al., 2007; Irvine-Fynn et al.,
81 2011; Dunning et al., 2013; Staines et al., 2015) and moraine development
82 (Chandler et al., 2015); the characterisation of glacier surface roughness (e.g. Sanz-
83 Ablanedo et al., 2012; Irvine-Fynn et al., 2014), sedimentology (Westoby et al.,
84 2015), and hydrology (Rippin et al., 2015); as well as input data for surface energy
85 balance modelling (e.g. Arnold et al., 2006; Reid et al., 2012); and for characterising
86 glacial landforms in formerly glaciated landscapes (e.g. Smith et al., 2009; Tonkin et
87 al., 2014; Hardt et al., 2015).

88

89 In this study, we utilise fine-resolution topographic datasets to quantify the surface
90 evolution of a blue-ice moraine complex in a remote part of Antarctica. Blue-ice
91 areas cover approximately 1% of Antarctica's surface area (Bintanja, 1999), yet they
92 remain relatively understudied. Relict blue-ice moraines preserved on nunataks are
93 key indicators of ice sheet elevation changes; however, limited data exist on rates
94 and patterns of surface reorganisation, which may be of use for contextualising the
95 results of, for example, cosmogenic nuclide dating and geomorphological mapping.
96 This research seeks to quantify the short-term surface evolution of a moraine
97 complex in Patriot Hills, Heritage Range, Antarctica (Fig. 1), through the differencing
98 and analysis of multi-temporal topographic datasets acquired using TLS and the
99 application of SfM-MVS photogrammetry to optical imagery acquired from a low-
100 altitude UAV sortie.

101

102 **2. Study site**

103

104 The study site is a blue-ice moraine complex, located on the northern flank of the
105 Patriot Hills massif at the southern-most extent of Heritage Range, West Antarctica
106 (Fig. 1). Blue-ice moraine formation is hypothesised to be the result of preferential
107 ablation of marginal ice by katabatic winds, which in turns prompts the modification
108 of ice flow and englacial sediment transport pathways such that basal sediment is
109 brought to the ice surface, where it is deposited (e.g. Bintanja, 1999; Sinisalo and
110 Moore, 2010; Fogwill et al., 2012; Spaulding et al., 2012; Hein et al., 2016). The site
111 comprises a series of broadly east-west oriented moraine ridges and inter-moraine
112 troughs, as well as an area of subdued moraine topography immediately adjacent to
113 the ice margin (Fig. 2). At this location, the active blue-ice moraines occupy an
114 altitudinal range of 60-70 m above the ice margin (~730 m a.s.l.), and extend for a
115 distance of up to 350 m into a bedrock embayment. The blue-ice moraines can be
116 traced for a distance of >4 km to the east and north-east, parallel to the range front,

117 and fill ice-marginal embayments. The site is geomorphologically and
118 sedimentologically complex (e.g. Vieira et al., 2012; Westoby et al., 2015), and,
119 along with moraine ridges and troughs, includes areas of subdued ice-marginal
120 topography with thermokarst melt ponds, local gullying and crevassing on ice-
121 proximal and distal moraine flanks, as well as solifluction deposits at the base of the
122 surrounding hillslopes. The bedrock hillslopes are overlain by a till drape with rare,
123 large exotic sandstone boulder erratics which have some evidence of periglacial
124 reworking. Field observations suggest that the blue-ice moraines are dynamic
125 features which are undergoing localised surface changes. It is these short-term,
126 changes which are the subject of investigation in this paper.

127

128 **3. Methods and data products**

129

130 This research employs two methods for reconstructing moraine surface topography,
131 specifically TLS and SfM-MVS photogrammetry. Two field campaigns at Patriot Hills
132 were undertaken with a 12-month survey interval. Briefly, TLS data were acquired at
133 the beginning and end of austral summer season 1 (December 2012 and January
134 2013, respectively), and in a short resurvey visit in season 2 (January 2014). Low-
135 altitude aerial optical photography was acquired from a UAV at the end of season 1
136 and was used as the primary input to SfM-MVS processing. The following sections
137 detail the two methods of topographic data acquisition, data processing, and
138 subsequent analysis using 'cloud-to-cloud' differencing.

139

140 **3.1. Topographic data acquisition**

141

142 **3.1.1. Terrestrial Laser Scanning**

143

144 TLS data were acquired using a Riegl LMS-Z620 time-of-flight laser scanner, set to
145 acquire ~11,000 points per second in the near-infrared band at horizontal and
146 vertical scanning increments of 0.031°, equivalent to a point spacing of 0.05 m at a
147 distance of 100 m and with a beam divergence of 15 mm per 100 m. Data were
148 acquired from six locations across the site at the beginning of season 1 (7th -11th
149 December 2012; Fig. 1; Table 1). Two of these positions were re-occupied at the
150 end of season 1 (9th January 2013) and three positions were reoccupied in season 2
151 (Fig. 1; 14th January 2014). Following manual editing and the automated removal of
152 isolated points to improve data quality, each set of scans were co-registered in Riegl
153 RiSCAN PRO software (v. 1.5.9) using a two-step procedure employing coarse
154 manual point-matching followed by the application of a linear, iterative, least-squares
155 minimisation solution to reduce residual alignment error. Individual scans were then

156 merged to produce a single 3D point cloud for each scan date. Merged scan data
157 from the end of seasons 1 and 2 were subsequently registered to the scan data from
158 the beginning of season 1 using the methods described above (Table 1).

159

160 **3.1.2. Structure-from-Motion with Multi-View Stereo photogrammetry**

161

162 Low-altitude aerial photographs of the study site were acquired using a 10-Megapixel
163 Panasonic Lumix DMC-LX5 compact digital camera with a fixed focal length (8 mm)
164 and automatic exposure settings, mounted in a fixed, downward-facing (nadir)
165 perspective on a sub-5 kg fixed-wing UAV. Photographs were acquired in a single
166 sortie lasting ~5 minutes. A total of 155 photographs were acquired at a 2-second
167 interval at an approximate ground height of 120 m, producing an average image
168 overlap of 80%, and an approximate ground resolution of 0.07 m² per pixel. Mean
169 point density was ~300 points per m², compared to a mean of 278 points per m² for
170 the TLS datasets. Motion blur of the input images was negligible due to favourable
171 image exposure conditions and an appropriate UAV flying height and speed.

172

173 UAV photographs were used as input to SfM reconstruction using the proprietary
174 Agisoft PhotoScan Professional Edition (v. 1.1.6) software. Unique image tie-points
175 which are stable under variations in view perspective and lighting are identified and
176 matched across input photographs, similar to Lowe's (2004) Scale Invariant Feature
177 Transform (SIFT) method. An iterative bundle adjustment algorithm is used to solve
178 for internal and external camera orientation parameters and produce a sparse 3D
179 point cloud. The results of the first-pass camera pose estimation were scrutinised
180 and only 3D points which appear in a minimum of 3 photographs and possessed a
181 reprojection error of <1.0 were retained. A two-phase method of UAV-SfM data
182 registration was employed: 1) ground control was obtained by identifying common
183 features in the UAV-SfM photographs and TLS data from the end of season 1
184 (acquired 4 days after the SfM data; Table 1), such as the corners of large, well-
185 resolved boulders. GCP data were used to optimise the initial camera alignment and
186 transform the regenerated UAV-SfM data to the same object space as the TLS data,
187 producing an xyz RMS error of 0.23 m. 2) following dense reconstruction, 3D point
188 data were exported to RiSCAN PRO (v. 1.5.9) software, and a linear, iterative, least-
189 squares minimisation employing surface plane matching was used to improve the
190 alignment and reduce the xyz RMS error to 0.03 m.

191

192 **3.2. Cloud-to-cloud differencing**

193

194 Three-dimensional ‘cloud-to-cloud’ distance calculations were used to quantify
195 moraine surface evolution (e.g. Lague et al., 2013). Since the dominant direction of
196 surface evolution across the study site was unknown *a priori*, the application of an
197 algorithm that is capable of detecting fully three-dimensional topographic change
198 was deemed to be the most appropriate method in this context. To this end, we
199 employ the Multiscale Model to Model Cloud Comparison (M3C2) algorithm (Lague
200 et al., 2013; Barnhart and Crosby, 2013), implemented in the open-source
201 CloudCompare software (v. 2.6.1) for change detection.

202

203 The M3C2 algorithm implements two main processing steps to calculate 3D change
204 between two point clouds: 1) estimation of surface normal orientation at a scale
205 consistent with local surface roughness, and 2) quantification of the mean cloud-to-
206 cloud distance (i.e. surface change) along the normal direction (or orthogonal
207 vector), which includes an explicit calculation of the local confidence interval. A point-
208 specific normal vector is calculated by fitting a plane to neighbouring 3D points that
209 are contained within a user-specified search radius. To avoid the fluctuation of
210 normal vector orientations and a potential overestimation of the distance between
211 two point clouds, the radius, or scale, used for normal calculation needs to be larger
212 than the topographic roughness, which is calculated as the standard deviation of
213 local surface elevations (σ). The orientation of the surface normal around a point, i , is
214 therefore dependent on the scale at which it is computed (Lague et al., 2013). A trial-
215 and-error approach was employed to reduce the estimated normal error, $E_{\text{norm}}(\%)$,
216 through refinement of a re-scaled measure of D , ξ , where:

217

$$218 \quad \xi(i) = \frac{D}{\sigma_i(D)} \quad \text{Eq. (1)}$$

219

220 Using this re-scaled measure of D , ξ can be used as an indicator of estimated normal
221 orientation accuracy, such that where ξ falls in the range ~ 20 -25, the estimated
222 normal error is $E_{\text{norm}} < 2\%$ (Lague et al., 2013). A fixed normal scaling of 2 m was
223 found to be sufficient to ensure that $\xi > 20$ for $>98\%$ of points in each topographic
224 dataset.

225

226 The radius of the projection cylinder, d , within which the average surface elevation of
227 each cloud is calculated, was specified as 2 m. This scaling ensured that the number
228 of points sampled in each cloud was ≥ 30 , following guidance provided by Lague et
229 al. (2013). M3C2 execution took ~ 0.3 h for each differencing task on a desktop
230 computer operating with 32 GB of RAM, and a 3.4 GHz CPU. Cloud-to-cloud
231 distances and statistics were projected onto the original point cloud. M3C2 output

232 was subsequently masked to exclude points where change is lower than level of
233 detection threshold for a 95% confidence level, $LoD_{95\%}(d)$, which is defined as:

234

$$235 \quad LoD_{95\%}(d) = \pm 1.96 \left(\frac{\sigma_1(d)^2}{n_1} + \frac{\sigma_2(d)^2}{n_2} + reg \right) \quad \text{Eq. (2)}$$

236

237 where d is the radius of the projection cylinder, reg is the user-specified registration
238 error, for which we substitute the propagated root mean square alignment error for
239 point clouds n_1 and n_2 (Table 2; Eq. (1)) and assume that this error is isotropic and
240 spatially uniform across the dataset.

241

242 To calculate the total propagated error for each differencing epoch, σ_{DoD} , the
243 estimates of errors in each point cloud (i.e. the sum of the average scan-scan RMS
244 error and a project-project RMS error, where applicable) were combined using:

245

$$246 \quad \sigma_{DoD} = \sqrt{\sigma_{C_1}^2 + \sigma_{C_2}^2} \quad \text{Eq. (3)}$$

247

248 where $\sigma_{C_1}^2$ and $\sigma_{C_2}^2$ are the RMS errors associated with point clouds C_1 and C_2 .

249

250

251 **3.3. Data intercomparison: SfM vs. TLS**

252

253 Whilst the UAV-SfM dataset acquired at the end of season 1 significantly improves
254 on the spatial coverage afforded by the use of TLS across the moraine embayment,
255 an analyses of the relative accuracy of the reconstructed surface topography of the
256 former is desirable. To this end, Fig. 3 shows the results of vertical differencing of the
257 UAV-SfM and TLS data, complemented by a series of surface elevation profiles (Fig.
258 4). These results reveal that 83% of the UAV-SfM data are within ± 0.1 m of the
259 equivalent TLS data, with a number of outliers at the northernmost margin of the
260 dataset, where the UAV-SfM data typically underestimate the TLS surface elevation.
261 Similarly, the UAV-SfM data underestimate the surface elevation of the ice-proximal
262 flank of the main moraine crest by, on average, ~ 0.13 m. UAV-SfM data
263 overestimate the moraine surface elevation in the north-western sector of the site by
264 ~ 0.12 m, with some outliers which exceed ~ 0.3 m.

265

266 Transect data also highlight areas of inconsistency, specifically often considerable
267 offsets between the TLS and SfM data which were collected at the end of season 1
268 and which, in places, approach 0.5 m in magnitude (e.g. at ~ 27 m distance in profile
269 A, and between 22-30 m in profile B; Fig. 4). Given that the SfM data were optimised

270 and georegistered using features extracted from the corresponding TLS dataset, one
271 might expect that deviations between the two would be barely discernible. However,
272 the SfM data variously over- and underestimate the TLS-derived surface elevation
273 with little apparent systematicity (Fig. 4). One potential explanation for these
274 inconsistencies could be the evolution of moraine surface topography in the 4-day
275 interval which separated the acquisition of the TLS and SfM data at the end of
276 season 1 (Table 1), with the implication that features used as GCPs in the TLS data
277 and their counterparts in the UAV-SfM data were not static, thereby affecting the
278 georeferencing and SfM optimisation solution. However, as we observe no clustering
279 of large GCP errors in areas of activity, this factor is unlikely to account for these
280 topographic inconsistencies.

281
282 An additional, and equally viable explanation for these inconsistencies might include
283 the near-parallel and largely nadir view directions of the UAV imagery, which
284 represent a largely 'non-convergent' mode of photograph acquisition that has
285 elsewhere been found to result in the deformation, or 'doming' of SfM-derived
286 surface topography (e.g. James and Robson, 2014; Rosnell and Honkavaara, 2012;
287 Javernick et al., 2014). Topographic mismatches between the TLS and UAV-SfM
288 data appear to be the most prominent in areas of steep topography (Fig. 3; Fig. 4).
289 These areas were generally well-resolved in the TLS data (where not topographically
290 occluded), but may have been resolved in less detail and with less accuracy in the
291 UAV-SfM data, where the fixed camera angle promotes the foreshortening of these
292 steep slopes in the aerial photography. Model deformations can be countered to
293 some degree through the inclusion of additional, oblique imagery, and use of suitable
294 GCPs (James and Robson, 2014). However, although the latter were relatively
295 evenly spaced across our study site, the inclusion of these data and subsequent use
296 for the optimisation of the SfM data prior to dense point cloud reconstruction does
297 not appear to have altogether eliminated these model deformations.

298
299

300 **4. Short-term topographic evolution of blue-ice moraines**

301

302 The results of 3D cloud-to-cloud differencing are summarised in Figure 5. Threshold
303 levels of change detection ranged from 0.094 – 0.103 m. The upper (i.e. most
304 conservative) bound of this range was applied to the results from all differencing
305 epochs, so that only 3D surface changes greater than 0.103 m were considered in
306 the subsequent analysis. The horizontal (xy) and vertical (z) components of 3D
307 surface change were separated to aid the analysis and interpretation of moraine
308 surface evolution. Vertical surface changes for a range of epochs, encompassing
309 intra-annual and annual change, are displayed in Fig. 5, whilst illustrative horizontal

310 components of 3D change are shown in Fig. 6. The longest differencing epoch,
311 representing a period of ~400 days (Fig. 5b) shows a broad pattern of net uplift
312 across the moraine of the order of 0.074 m. Locally, uplift exceeds 0.2 m across
313 parts of the moraine complex, and, whilst on first glance these elevation gains
314 appear to be largely randomly distributed across the site, on closer inspection they
315 occur predominantly on or adjacent to the main, central moraine ridge and close to
316 the current ice margin. The large central moraine ridge exhibits a mean uplift of 0.11
317 m, whilst specific ice-marginal areas to the west and an area of moraine to the south-
318 west of the embayment also exhibit uplift of a similar magnitude (Fig. 5b). In contrast,
319 an area in the southernmost sector of the basin and an ice-marginal area to the
320 centre-west exhibit a net reduction in moraine surface elevation, up to a maximum of
321 -0.354 m.

322

323 Intra-annual change detection mapping was undertaken using TLS-TLS and TLS-
324 SfM differencing (Fig. 5c, d). Key similarities between these two datasets, which
325 represent vertical topographic change over a ~31 and ~27 day period, respectively,
326 include uplift at the southern extent of the embayment (mean 0.081 m and 0.123 m
327 for the TLS-TLS and TLS-SfM differencing, respectively). Similarly, both datasets
328 reveal surface lowering at south-eastern, or true rear, of the basin (mean -0.106 m
329 and -0.112 m for TLS-SfM and TLS-TLS differencing, respectively), and, in the TLS-
330 SfM data, on the ice-distal (southern) side of the central moraine ridge (Fig. 5c; -
331 0.092 m). However, the large area of ice-marginal surface lowering (-0.095 - -0.373
332 m) that is detected in the TLS-SfM differencing results is not mirrored in the
333 equivalent TLS-TLS differencing data (Fig. 5d). This stems in large part from the
334 reduced spatial coverage of the usable TLS scan data acquired at the end of season
335 1, which comprised data from only two scan positions (Fig. 1c) and which omits the
336 ice-marginal zone.

337

338 The results of vertical change detection using both SfM-TLS and TLS-TLS
339 approaches also display similarities for differencing undertaken between the end of
340 season 1, and season 2 (Fig. 5e,f), including a largely continuous area of uplift
341 across the centre of the site, as well as areas of surface lowering along the eastern
342 edge of the site. Whilst widespread uplift characterises the entire western edge of
343 the study area in the TLS-TLS data (Fig. 5f), the equivalent SfM-TLS data instead
344 report the occurrence of surface lowering at the base of the hillslope spur which
345 forms the western boundary of the site (Fig. 5e). Furthermore, an area of
346 considerable (mean 0.218 m) uplift characterises the ice-marginal zone in the SfM-
347 TLS differencing data for this epoch, but, once again, the reduced spatial coverage
348 of the TLS datasets mean that no differencing data are available to verify or contest

349 this pattern. However, we note that vertical change at the ice-marginal (northern)
350 limit of the TLS-TLS data for both intra-annual and annual differencing epochs do not
351 correspond with the equivalent SfM-TLS / TLS-SfM results.

352

353 Examples of horizontal displacement, calculated here as the *xy* component of the
354 orthogonal distance between two point clouds acquired at separate times, and
355 gridded to represent the average *xy* displacement within 10 m² grid cells, are shown
356 in Fig. 6 for intra- (Fig. 6a) and inter-annual epochs (Fig. 6b). Within season 1, a
357 range of *xy* displacement orientations are detected, and range from sub-centimetre
358 to >0.2 m in magnitude. These displacements include extensive southern (or
359 'inward') movement of the moraine surface in the ice-marginal zone, which is
360 associated with surface lowering, and which grades into a largely western-oriented
361 displacement signal on the ridgeline of the main moraine crest and across the
362 western sector of the moraine complex (Fig. 6a). Total *xy* displacement over a >1
363 year period (Fig. 6b) appears to be less uniform and comparatively chaotic.
364 However, a number of local and largely consistent patterns of horizontal
365 displacement are discernible, such as predominantly westward movement along the
366 central moraine ridge, and north- to north-eastern motion along the western edge of
367 the site (Fig. 6b), which also occurs within season 1 (Fig. 6a). Both trends are
368 associated with net surface uplift. In contrast, isolated patches of surface lowering
369 are generally characterised by southern or south-westerly *xy* displacement.

370

371 The analysis of a series of surface profile transects which bisect the moraines shed
372 further light on their topographic evolution (Fig. 4). These data are particularly useful
373 for examining the interplay between vertical and lateral moraine surface
374 displacement, which is alluded to in Fig. 6. For example, a combination of surface
375 uplift and lateral displacement between the start and end of season 1 is visible
376 between 28-40 m in profile A (Fig. 4, inset 1). Similarly, lateral (southern) translation
377 of the moraine surface between 15-22 m in profile C (Fig. 4, inset 2) is visible for the
378 same differencing epoch.

379

380 **5. Implications for glaciological process analysis**

381

382 Here we highlight some implications arising from the measurement of these short-
383 term changes in surface morphology. Topographically, the Patriot Hills blue-ice
384 moraine confirms the morphological observations of the embayment, described by
385 Fogwill et al. (2012) as comprising sloping terraces and blocky, pitted boulder
386 moraine ridges. These ridges are thought to be fed from beneath by steeply dipping
387 debris bands coming from depth, driven by ice-flow compensating for katabatic wind

388 ablation of the glacier. Vieira et al. (2012) classify what we term blue-ice moraines as
389 'supraglacial moraine', and the debris bands in the blue ice outside of the basin as
390 blue-ice moraines. It is from clasts emerging from these bands that Fogwill et al.
391 (2012) have produced their model of blue-ice moraine formation in the basin. The
392 supraglacial moraines of Vieira et al. (2012) are described as slightly creeping
393 debris-mantled slopes – both Fogwill et al. (2012) and Vieira et al. (2012) consider
394 the features in the basin as active, but without measurements of observations of
395 rates, or the nature of change. Our differencing results confirm the hypothesis that
396 these features are active, and develops this idea further to demonstrate that moraine
397 slope evolution is active over annual to intra-annual timescales.

398

399 Hättestrand and Johansen (2005) discussed the evolution of blue-ice moraine
400 complexes in Dronning Maud Land, Antarctica, and hypothesised that, following ice-
401 marginal deposition of debris when the adjacent ice surface was higher, the
402 subsequent lowering of the exposed ice surface would produce a slope 'outwards'
403 from an embayment, followed by gradual movement of material towards the ice-
404 margin in a manner similar to that exhibited by active rock glaciers – features that
405 Vieira et al. (2012) interpret in the next basin along the Patriot Hills range. However,
406 whilst the former holds true as an explanation for the general gradient of the Patriot
407 Hills moraine complex (e.g. Fig. 4), our results suggest that the short-term evolution
408 of the moraines does not necessarily conform to the latter hypothesis of such as
409 simple process of consistent downslope movement, and in fact exhibits far more
410 dynamic complexity.

411

412 The moraine ridges both close to, and far from the ice margin emerge as axes of
413 activity and uplift (Fig. 5c), despite initial field observations suggesting that the ridges
414 most distant from the exposed ice surface were older and less active. Fogwill et al.
415 (2012) suggest that once upcoming debris is at a sufficient thickness, wind-driven
416 ablation shuts off. Our observations suggest that if this is the case, these ridges are
417 not left stagnant at this point. The interplay between ice flow and surface elevation
418 lowering by wind, but reduced by thicker debris, continues despite the possible ages
419 of the surface debris relative to ridges closer to the contemporary blue-ice margin.
420 This activity is not simply confined to '*inward*' or '*outward*' movement of moraines
421 within the embayment, but also involves a lateral component. It is notable that most
422 lowering occurred near the ice margin where the debris layer is typically thinnest and
423 less than ~0.15 m. Surface lowering in this area exceeds 0.3 m within season 1 (Fig.
424 5c), and may be the result of sub-debris ice ablation, which promotes terrain
425 relaxation and has been widely reported in other ice-proximal landscapes (e.g.

426 Krüger and Kjær, 2000; Schomacker, 2008; Irvine-Fynn et al., 2011; Staines et al.,
427 2015).

428

429 Lateral movement within the moraine ridges (Fig. 6) may reflect lateral extension or
430 'stretching' of the ridges as they encroach into the embayment. Such lateral
431 movement is corroborated from the orientation of crevasse-based grooves in the
432 moraine (Fig. 2c). The apparent inward encroachment of the Patriot Hills moraines
433 may be the product of the pressure exerted on the moraines by glacier ice flow into
434 the embayment in compensation for preferential ice ablation by katabatic winds,
435 which is consistent with blue-ice moraine formation theory (Fogwill et al., 2012).
436 Finally, the close match of inter-season surface elevation cross-profiles (Fig. 5)
437 points to medium-term stability of the moraine system. This conclusion will be
438 investigated through the application of cosmogenic isotope evidence to assess
439 change since the Holocene.

440

441 More broadly, this study has demonstrated the potential for the combination of
442 different high-resolution surveying technologies and advanced, 3D topographic
443 differencing methods for elucidating the short-term evolution of glaciated landscapes.
444 Whilst this study has focused exclusively on the surface evolution of Antarctic blue-
445 ice moraines, the application of 3D differencing methods to quantify change between
446 repeat, accurate topographic surveys has a wide range of potential glaciological
447 applications, which cryospheric researchers have already begun to capitalise on
448 (e.g. Piermattei et al., 2015, Gabbud et al., 2015; Kraaijenbrink et al., 2016). A key
449 contribution of this study to the wider Earth surface dynamics community is the
450 demonstration of truly 3D differencing methods to reveal not only vertical surface
451 change, but also the magnitude and direction of any lateral component to surface
452 movement. Such methods may have particular value for quantifying the 3D surface
453 evolution of, for example, rock glaciers, degrading ice-cored moraines, or slope
454 instabilities in permafrost regions, where information regarding both vertical and
455 lateral components of landscape development may be both of scientific interest and
456 practical application.

457

458 **6. Summary**

459

460 This research has employed a combination of TLS and UAV-based SfM-MVS
461 photogrammetry and 3D differencing methods to quantify the topographic evolution
462 of an Antarctic blue-ice moraine complex over annual and intra-annual timescales.
463 Segmentation of lateral and vertical surface displacements reveal site- and local-
464 scale patterns of geomorphometric moraine surface evolution beyond a threshold

465 level of detection (95% confidence), including largely persistent vertical uplift across
466 key moraine ridges, both within a single season, and between seasons. This
467 persistent uplift is interspersed with areas (and periods) of surface downwasting
468 which is largely confined to the rear of the moraine basin for both differencing
469 epochs, and in ice-marginal regions within season 1. Analysis of lateral displacement
470 vectors, which are generally of a much smaller magnitude than vertical
471 displacements, provide further insights into moraine surface evolution.

472

473 A number of methodological shortcomings are highlighted. Briefly, these relate to the
474 incomplete spatial coverage afforded by the use of TLS in a topographically complex
475 environment, and issues associated with obtaining suitable ground control for SfM-
476 MVS processing and potential implications for the accuracy of SfM-derived
477 topographic data products. This research represents the first successful application
478 of a combination of high-resolution surveying methods for quantifying the
479 topographic evolution of ice-marginal topography in this environment. Furthermore,
480 we have demonstrated that, whilst a number of operational considerations must be
481 taken into account at the data collection stage, these technologies are highly
482 appropriate for reconstructing moraine surface topography and for quantifying Earth
483 surface evolution in glaciated landscapes more generally.

484

485

486 **Author contribution**

487

488 S. A. Dunning, J. Woodward, A. Hein, K. Winter, S. M. Marrero and D. E. Sugden
489 collected field data. TLS and SfM data processing and differencing were undertaken
490 by M. J. Westoby. Data analysis was performed by M. J. Westoby, S. A. Dunning
491 and J. Woodward. Manuscript figures were produced by M. J. Westoby. All authors
492 contributed to the writing and revision of the manuscript.

493

494 **Acknowledgements**

495

496 The research was funded by the UK Natural Environment Research Council
497 (Research Grants NE/I027576/1, NE/I025840/1, NE/I024194/1, NE/I025263/1). We
498 thank the British Antarctic Survey for logistical support.

499 **References**

500

501 Agisoft: Agisoft PhotoScan Professional Edition v.1.1.6. Available:
502 <http://www.agisoft.com>, 2014.

503

504 Arnold, N. S., Rees, W. G., Hodson, A. J., and Kohler, J.: Topographic controls on
505 the surface energy balance of a high Arctic valley glacier. *Journal of Geophysical*
506 *Research*, 111, F02011, doi: 10.1029/2005JF000426, 2006.

507

508 Baltasvias, E. P., Favey, E., Bauder, A., Bösch, H., and Pateraki, M.: Digital surface
509 modelling by airborne laser scanning and digital photogrammetry for glacier
510 monitoring. *Photogrammetric Record*, 17, 243-273, doi: 10.1111/0031-868X.00182,
511 2001

512

513 Barnhart, T. B. and Crosby, B. T.: Comparing two methods of surface change
514 detection on an evolving thermokarst using high-temporal-frequency terrestrial laser
515 scanning, Selawik River, Alaska. *Remote Sensing*, 5, 2813-2837, doi:
516 10.3390/rs5062813, 2013.

517

518 Bhardwaj, A., Sam, L., Akanksha, Martín-Torres, F.J., and Kumar, R.: UAVs as
519 remote sensing platform in glaciology: Present applications and future prospects.
520 *Remote Sensing of Environment*, 175, 196-204, doi: 10.1016/j.rse.2015.12.029,
521 2016.

522

523 Bintanja, R.: On the glaciological, meteorological, and climatological significance of
524 Antarctic blue ice areas. *Reviews of Geophysics*, 37, 337-359, doi:
525 10.1029/1999RG900007, 1999.

526

527 Bollmann, E., Sailer, R., Briese, C., Stotter, J., and Fritzmann, P.: Potential of
528 airborne laser scanning for geomorphologic feature and process detection and
529 quantifications in high alpine mountains. *Zeitschrift für Geomorphologie*, 55, 83-104,
530 doi: 10.1127/0372-8854/2011/0055S2-0047, 2011.

531

532 Brasington, J., Rumsby, B. T., and McVey, R. A.: Monitoring and modelling
533 morphological change in a braided gravel-bed river using high resolution GPS-based
534 survey. *Earth Surface Processes and Landforms*, 25, 973-990, doi: 10.1002/1096-
535 9837(200008)25:9<973::AID-ESP111>3.0.CO;2-Y, 2000.

536

537 Chandler, B. M. P., Evans, D. J. A., Roberts, D. H., Ewertowski, M., and Clayton, A.
538 I.: Glacial geomorphology of the Skálafellsjökull foreland, Iceland: A case study of
539 'annual' moraines. *Journal of Maps*, doi: 10.1080/17445647.2015.1096216, 2015.

540

541 Dunning, S. A., Large, A. R. G., Russell, A. J., Roberts, M. J., Duller, R., Woodward,
542 J., Mériaux, A-S., Tweed, F. S., and Lim, M.: The role of multiple glacier outburst
543 floods in proglacial landscape evolution: The 2010 Eyjafjallajökull eruption, Iceland.
544 *Geology*, 796 41(10), 1123-1136, doi: 10.1130/G34665, 2013.

545

546 Farr, T. G., Rosen, P. A., Caro, E., Crippen, R., Duren, R., Hensley, S., Kobrick, M.,
547 Paller, M., Rodriguez, E., Roth, L., Seal, D., Shaffer, S., Shimada, J., Umland, J.,
548 Werner, M., Oskin, M., Burbank, D., and Alsdorf, D.: The shuttle radar topography

549 mission. *Reviews of Geophysics*, 45(2), RG2004, doi: 10.1029/2005RG000183,
550 2007.

551

552 Fogwill, C. J., Hein, A. S., Bentley, M. J., and Sugden, D. E.: Do blue-ice moraines in
553 the Heritage Range show the West Antarctic ice sheet survived the last interglacial?
554 *Palaeogeography, Palaeoclimatology, Palaeoecology*, 335-336, 61-70, doi:
555 10.1016/j.palaeo.2011.01.027, 2012.

556

557 Fuller, I. C., Large, A. R. G., and Milan, D.: Quantifying channel development and
558 sediment transfer following chute cutoff in a wandering gravel-bed river.
559 *Geomorphology*, 54, 307-323, doi: 10.1016/S0169-555X(02)00374-4, 2003.

560

561 Gabbud, C., Micheletti, N., and Lane, S. N.: Lidar measurement of surface melt for a
562 temperate Alpine glacier at the seasonal and hourly scales. *Journal of Glaciology*,
563 61(229), 963-974, doi: 10.3189/2015JoG14J226, 2015.

564

565 Hardt, J., Hebenstreit, R., Lüthgens, C., and Böse, M.: High-resolution mapping of
566 ice-marginal landforms in the Barnim region, northeast Germany. *Geomorphology*,
567 250, 41-52, doi: 10.1016/j.geomorph.2015.07.045, 2015.

568

569 Hättestrand, C., and Johansen, N.: Supraglacial moraines in Scharffenbergbotnen,
570 Heimafrontfjella, Dronning Maud Land, Antarctica – significance for reconstructing
571 former blue ice areas. *Antarctic Science*, 17(2), 225-236, doi:
572 10.1017/S0954102005002634, 2005.

573

574 Hein, A.S., Woodward, J., Marrero, S.M., Dunning, S.A., Steig, E.J., Freeman,
575 S.P.H.T., Stuart, F.M., Winter, K., Westoby, M.J., and Sugden, D.E.: Evidence for
576 the stability of the West Antarctic Ice Sheet divide for 1.4 million years. *Nature*
577 *Communications*, 7, 10325, doi: 10/1038/ncomms10325, 2016.

578

579 Hodge, R., Brasington, J., and Richards, K.: In-situ characterisation of grain-scale
580 fluvial morphology using Terrestrial Laser Scanning. *Earth Surface Processes and*
581 *Landforms*, 34, 954-968, doi: 10.1002/esp.1780, 2009.

582

583 Immerzeel, W. W., Kraaijenbrink, P. D. A., Shea, J. M., Shrestha, A. B., Pellicciotti,
584 F., Bierkens, M. F. P., and de Jong, S. M.: High-resolution monitoring of Himalayan
585 glacier dynamics using unmanned aerial vehicles. *Remote Sensing of Environment*,
586 150, 93-103, doi: 10.1016/j.rse.2014.04.025, 2014.

587

588 Irvine-Fynn, T. D. L., Sanz-Ablanedo, E., Rutter, N., Smith, M. W., and Chandler, J.
589 H.: Measuring glacier surface roughness using plot-scale, close-range digital
590 photogrammetry. *Journal of Glaciology*, 60(223), 957-969, doi:
591 10.3189/2014JoG14J032, 2014.

592

593 James, M. R., and Robson, S.: Straightforward reconstruction of 3D surfaces and
594 topography with a camera: accuracy and geoscience application. *Journal of*
595 *Geophysical Research*, 117, F03017, doi: 10.1029/2011JF002289, 2012.

596

597 James, M. R. and Robson, S.: Mitigating systematic error in topographic models
598 derived from UAV and ground-based image networks. *Earth Surface Processes and*
599 *Landforms*, 39, 1413-1420, doi: 10.1002/esp.3609, 2014.
600

601 James, M. R., Robson, S., Pinkerton, H., and Ball, M.: Oblique photogrammetry with
602 visible and thermal images of active lava flows. *Bulletin of Volcanology*, 69, 105-108,
603 doi: 10.1007/200445-006-0062-9, 2006.
604

605 Javernick, L., Brasington, J., and Caruso, B.: Modelling the topography of shallow
606 braided rivers using Structure-from-Motion photogrammetry. *Geomorphology*, 213,
607 116-182, doi: 10.1016/j.geomorph.2014.01.006, 2014.
608

609 Kääb, A.: Monitoring high-mountain terrain deformation from repeated air- and
610 spaceborne optical data: examples using digital aerial imagery and ASTER data.
611 *ISPRS Journal of Photogrammetry and Remote Sensing*, 57(1-2), 39-52, doi:
612 10.1016/S0924-2716(02)00114-4, 2002.
613

614 Kääb, A., Girod, L., and Berthling, L.: Surface kinematics of periglacial sorted circles
615 using structure-from-motion technology. *The Cryosphere*, 8, 1041-1056, doi:
616 10.5194/tc-8-1041-2014, 2014.
617

618 Keim, R. F., Skaugset, A. E., and Bateman, D. S.: Digital terrain modelling of small
619 stream channels with a total-station theodolite. *Advances in Water Resources*, 23,
620 41-48, doi: 10.1016/S0309-1708(99)00007-X, 1999.
621

622 Keutterling, A. and Thomas, A.: Monitoring glacier elevation and volume changes
623 with digital photogrammetry and GIS at Gepatschferner glacier, Austria. *International*
624 *Journal of Remote Sensing*, 27(19), 4371-4380, doi: 10.1080/01431160600851819,
625 2006.
626

627 Kraaijenbrink, P., Meijer, S. W., Shea, J. M., Pellicciotti, F., de Jong, S. M., and
628 Immerzeel W. W.: Seasonal surface velocities of a Himalayan glacier derived by
629 automated correlation of unmanned aerial vehicle imagery. *Annals of Glaciology*,
630 57(71), 103-113, doi: 10.3189/2016AoG71A072, 2016.
631

632 Krüger, J., and Kjær, K.H.: De-icing progression of ice-cored moraines in a humid,
633 subpolar climate, Kötlujökull, Iceland. *The Holocene*, 10(6), 737-747, doi:
634 10.1191/09596830094980, 2000.
635

636 Lague, D., Brodu, N., and Leroux, J.: Accurate 3D comparison of complex
637 topography with terrestrial laser scanner: Application to the Rangitikei canyon (N-Z).
638 *ISPRS Journal of Photogrammetry and Remote Sensing*, 82, 10-26, doi:
639 10.1016/j.isprsjprs.2013.04.009, 2013.
640

641 Lewis, A., Hilley, G. E., and Lewicki, J. L.: Integrated thermal infrared imaging and
642 structure-from-motion photogrammetry to map apparent temperature and radiant
643 hydrothermal heat flux at Mammoth Mountain, CA, USA. *Journal of Volcanology and*
644 *Geothermal Research*, 303, 16-24, doi: 10.1016/j.jvolgeores.2015.07.025, 2015.
645

646 Lowe, D. G.: Distinctive image features from scale-invariant keypoints. *International*
647 *Journal of Computer Vision*, 60(2), 91-110, doi:
648 10.1023/B%VISI.0000029664.99615.94, 2004.
649

650 Micheletti, N., Chandler, J. H., and Lane, S. N.: Investigating the geomorphological
651 potential of freely available and accessible structure-from-motion photogrammetry
652 using a smartphone. *Earth Surface Processes and Landforms*, 40(4), 473-486, doi:
653 10.1002/esp.3648, 2014.
654

655 Micheletti, N., Lane, S. N., and Chandler, J. H.: Application of archival aerial
656 photogrammetry to quantify climate forcing of Alpine landscapes. *The*
657 *Photogrammetric Record*, 30(150), 143-165, doi: 10.1111/phor.12099, 2015.
658

659 Milan, D. J., Heritage, G. L., and Hetherington, D.: Application of a 3D laser scanner
660 in the assessment of erosion and deposition volumes and channel change in a
661 proglacial river. *Earth Surface Processes and Landforms*, 32, 1657-1674, doi:
662 10.1002/esp.1592, 2007.
663

664 Niethammer, U., Rothmund, S., James, M. R., Traveletti, J., and Joswig, M.: UAV-
665 based remote sensing of landslide. *International Archives of the Photogrammetry,*
666 *Remote Sensing and Spatial Information Sciences*, 38(5), 496-501, doi:
667 10.1016/j.enggeo.2011.03.012, 2010.
668

669 Noh, M-J. and Howat, I. M.: Automated stereo-photogrammetric DEM generation at
670 high latitudes: Surface Extraction with TIN-based Search-space Minimization
671 (SETSM) validation and demonstration over glaciated regions. *GIScience and*
672 *Remote Sensing*, 52(2), doi: 10.1080/15481603.2015.1008621, 198-217, 2015.
673

674 Ouédraogo, M. M., Degré, A., Debouche, C., and Lisein, J.: The evaluation of
675 unmanned aerial system-based photogrammetry and terrestrial laser scanning to
676 generate DEMs of agricultural watersheds. *Geomorphology*, 214, 339-355, doi:
677 10.1016/j.geomorph.2014.02.016, 2014.
678

679 Passalacqua, P., Hillier, J., and Tarolli, P.: Innovative analysis and use of high-
680 resolution DTMs for quantitative interrogation of Earth-surface processes. *Earth*
681 *Surface Processes and Landforms*, 39, 1400-1403, doi: 10.1002/esp.3616, 2014.
682

683 Passalacqua, P., Belmont, P., Staley, D. M., Simley, J. D., Arrowsmith, J. R., Bode,
684 C. A., Crosby, C., DeLong, S. B., Glenn, N. F., Kelly, S. A., Lague, D., Sangireddy,
685 H., Schaffrath, K., Tarboton, D. G., Wasklewicz, T., and Wheaton, J. M.: Analyzing
686 high resolution topography for advancing the understanding of mass and energy
687 transfer through landscapes: A review. *Earth-Science Reviews*, 148, 174-193, doi:
688 10.1016/j.earscirev.2015.05.012, 2015.
689

690 Pepin, N. C., Duane, W. J., Schaefer, M., Pike, G., and Hardy, D. R.: Measuring and
691 modeling the retreat of the summit ice fields on Kilimanjaro, East Africa. *Arctic,*
692 *Antarctic and Alpine Research*, 46(4), 905-917, doi: 10.1657/1938-4246-46.4.905,
693 2014.
694

695 Piermattei, L., Carturan, L., and Guarnieri, A.: Use of terrestrial photogrammetry
696 based on structure-from-motion for mass balance estimation of a small glacier in the
697 Italian alps. *Earth Surface Processes and Landforms*, 40, 1791-1802, doi:
698 10.1002/esp.3756, 2015.

699
700 Pitkänen, T. and Kajuutti, K.: Close-range photogrammetry as a tool in glacier
701 change detection. *International Archives of the Photogrammetry, Remote Sensing
702 and Spatial Information Sciences (ISPRS)*, 35, 769-773, 2004.

703
704 Reid, T. D., Carenzo, M., Pellicciotti, F., and Brock, B. W.: Including debris cover
705 effects in a distributed model of glacier ablation. *Journal of Geophysical Research:
706 Atmospheres*, 117, D18105, doi: 10.1029/2012JD017795, 2012.

707
708 Rippin, D. M., Pomfret, A., and King, N.: High resolution mapping of supra-glacial
709 drainage pathways reveals links between micro-channel drainage density, surface
710 roughness and surface reflectance. *Earth Surface Processes and Landforms*,
711 40(10), 1279-1290, doi: 10.1002/esp.3719, 2015.

712
713 Rosnell, T. and Honkavaara, E.: Point cloud generation from aerial image data
714 acquired by a quadcopter type micro unmanned aerial vehicle and a digital still
715 camera. *Sensors*, 12, 453-480, doi: 10.3390/s120100453, 2012.

716
717 Rosser, N. J., Petley, D. N., Lim, M., Dunning, S. A., and Allison, R. J.: Terrestrial
718 laser scanning for monitoring the process of hard rock coastal cliff erosion. *Quarterly
719 Journal of Engineering Geology & Hydrogeology*, 38, 363-375, 2005.

720
721 Ryan, J. C., Hubbard, A. L., Box, J. E., Todd, J., Christoffersen, P., Carr, J. R., Holt,
722 T. O., and Snooke, N.: UAV photogrammetry and structure from motion to assess
723 calving dynamics at Store Glacier, a large outlet draining the Greenland ice sheet.
724 *The Cryosphere*, 9, 1-11, doi: 10.5194/tc-9-1-2015, 2015.

725
726 Sanz-Ablanedo, E., Chandler, J. H., and Irvine-Fynn, T. D. L.: Studying glacial melt
727 processes using sub-centimeter DEM extraction and digital close-range
728 photogrammetry. *ISPRS Archives*, 39(B5), 435-440, 2012.

729
730 Schomacker, A.: What controls dead-ice melting under different climate conditions?
731 A discussion. *Earth-Science Reviews*, 90, 103-113, doi:
732 10.1016/j.earscirev.2008.08.003, 2008.

733
734 Schwalbe, E. and Maas, H. G.: Motion analysis of fast flowing glaciers from multi-
735 temporal terrestrial laser scanning. *Photogrammetrie Fernerkundung
736 Geoinformation*, 1, 91-98, doi: 10.1127/0935-1221/2009/0009, 2009.

737
738 Sinisalo, A. and Moore, J. C.: Antarctic blue ice area – towards extracting
739 paleoclimate information. *Antarctic Science*, 22(2), 99-115, doi:
740 10.107/S0954102009990691, 2010.

741
742 Smith, M. J., Rose, J., and Booth, S.: Geomorphological mapping of glacial
743 landforms from remotely sensed data: An evaluation of the principal data sources

744 and an assessment of their quality. *Geomorphology*, 76(1-2), 148-165, doi:
745 10.1016/j.geomorph.2005.11.001, 2006.

746

747 Smith, M. J., Rose, J., and Gousie, M. B.: The Cookie Cutter: A method for obtaining
748 a quantitative 3D description of glacial bedforms. *Geomorphology*, 108, 209-218, doi:
749 10.1016/j.geomorph.2009.01.006, 2009.

750

751 Smith, M. W. and Vericat, D.: From experimental plots to experiment landscapes:
752 topography, erosion and deposition in sub-humid badlands from Structure-from-
753 Motion photogrammetry. *Earth Surface Processes and Landforms*, doi:
754 10.1002/esp.3747, 2015.

755

756 Spaulding, N. E., Spikes, V. B., Hamilton, G. S., Mayewski, P. A., Dunbar, N. W.,
757 Harvey, R. P., Schutt, J., and Kurbatov, A. V.: Ice motion and mass balance at the
758 Allan Hills blue-ice area, Antarctica, with implications for paleoclimate
759 reconstructions. *Journal of Glaciology*, 58(208), 399-406, doi:
760 10.3189/2012JoG11J176, 2012.

761

762 Staines, K. E. H., Carrivick, J. L., Tweed, F. S., Evans, A. J., Russell, A. J.,
763 Jóhannesson, T., and Roberts, M.: A multi-dimensional analysis of pro-glacial
764 landscape change at Sólheimajökull, southern Iceland. *Earth Surface Processes and*
765 *Landforms*, 40, 809-822, doi: 10.1002/esp.3662, 2015.

766

767 Stumpf, A., Malet, J-P., Allemand, P., and Ulrich, P.: Surface reconstruction and
768 landslide displacement measurements with Pléiades satellite images. *ISPRS Journal*
769 *of Photogrammetry and Remote Sensing*, 95, 1-12, doi:
770 10.1016/j.isprsjprs.2014.05.008, 2014.

771

772 Tarolli, P.: High-resolution topography for understanding Earth surface processes:
773 Opportunities and challenges. *Geomorphology*, 216, 295-312, doi:
774 10.1016/j.geomorph.2014.03.008, 2014.

775

776 Tonkin, T. N., Midgley, N. G., Graham, D. J., and Labadz, J. C.: The potential of
777 small unmanned aircraft systems and structure-from-motion for topographic surveys:
778 a test of emerging integrated approaches at Cwm Idwal, North Wales.
779 *Geomorphology*, 226, 35-43, doi: 10.1016/j.geomorph.2014.07.021, 2014.

780

781 Vieira, R., Hinata, S., da Rosa, K. K., Zilberstein, S., and Simoes, J. C.: Periglacial
782 features in Patriot Hills, Ellsworth Mountains, Antarctica. *Geomorphology*, 155-156,
783 96-101, doi: 10.1016/j.geomorph.2011.12.014, 2012.

784

785 Westoby, M. J., Brasington, J., Glasser, N. F., Hambrey, M. J., and Reynolds, J. M.:
786 'Structure-from-Motion' photogrammetry: A low-cost, effective tool for geoscience
787 applications. *Geomorphology*, 179, 300-314, doi: 10.1016/j.geomorph.2012.08.021,
788 2012.

789

790 Westoby, M. J., Dunning, S. A., Woodward, J., Hein, A. S., Marrero, S. M., Winter,
791 K., and Sugden, D. E.: Sedimentological characterisation of Antarctic moraines
792 using UAVs and Structure-from-Motion photogrammetry. *Journal of Glaciology*,
793 61(230), 1088-1102, doi: 10.3189/2015JoG15J086, 2015.

794

795 Wheaton, J. M., Brasington, J., Darby, S. E., and Sear, D. A.: Accounting for
796 uncertainty in DEMs from repeat topographic surveys: improved sediment budgets.
797 *Earth Surface Processes and Landforms*, 35, 136-156, doi: 10.1002/esp.1886, 2010.

798

799 Whitehead, K., Moorman, B., and Wainstein, P.: Measuring daily surface elevation
800 and velocity variations across a polythermal arctic glacier using ground-based
801 photogrammetry. *Journal of Glaciology*, 60(224), 1208-1220, doi:
802 10.3189/2014JoG14J080, 2014.

803

804 Woodget, A. S., Carbonneau, P. E., Visser, F., and Maddock, I. P.; Quantifying
805 submerged fluvial topography using hyperspatial resolution UAS imagery and
806 structure from motion photogrammetry. *Earth Surface Processes and Landforms*,
807 40(1), 47-64, doi: 10.1002/esp.3613, 2015.

808

Field survey	Scan position	Scan date	Scan-scan registration error (RMS; m)	Project-project registration error (RMS; m)
Season 1 start (TLS)	1	07 Dec 2012	Static	Static
	2	08 Dec 2012	0.0327	
	3	08 Dec 2012	0.0391	
	5	09 Dec 2012	0.0301	
	6	01 Dec 2012	0.0258	
	7	11 Dec 2012	0.0258	
	Season 1 end (TLS)	1	09 Jan 2013	Static
2		09 Jan 2013	0.0145	
Season 1 end (UAV-SfM)	-	05 Jan 2013	-	0.0306
Season 2 (TLS)	1	14 Jan 2014	Static	0.0149
	2	14 Jan 2014	0.0205	
	3	14 Jan 2014	0.0255	

810 **Table 2**
811

Differencing epoch	Propagated error (RMS; m)	M3C2 $LoD_{95\%}$ (m)
S1 start (TLS) - S1 end (TLS)	0.049	0.098
S1 start (TLS) - S1 end (SfM)	0.050	0.103
S1 end (TLS) - S2 end (TLS)	0.048	0.098
S1 end (SfM) - S2 end (TLS)	0.049	0.102
S1 start (TLS) - S2 end (TLS)	0.050	0.099

812 **Figure captions**

813

814 **Figure 1.** Blue-ice moraine embayment, Patriot Hills, Heritage Range, Antarctica. **(a)**
815 Geographical context of Patriot Hills within the Heritage Range, southern Ellsworth
816 Mountains. **(b)** The Patriot Hills massif. The location of the study embayment and
817 area displayed in **(c)** is highlighted in red. **(c)**: Detailed study site overview map.
818 Contours and underlying hillshade are derived from a UAV-SfM-derived DEM. TLS
819 positions for the start of season 1 are shown in red, blue and yellow. The two scan
820 positions re-occupied at the end of season 1 are shown in blue, whilst the three scan
821 positions reoccupied in season 2 are shown in blue and red. Background to **(a)** ©
822 U.S. Geological Survey, **(b)** 2015 DigitalGlobe, both extracted from Google Earth.

823

824 **Figure 2.** Field photographs of the Patriot Hills blue-ice moraine study site. **(a)**
825 Panoramic photograph of the moraine embayment – view north-east towards the ice
826 margin from the rear of the embayment. Area shown in **(c)** and position and view
827 direction of camera **(b)** shown for reference. **(b)** View to the north-west with moraine
828 crest in foreground and subdued, ice-marginal moraine surface topography in
829 middle-ground. **(c)** Close-up of moraine topography, highlighting ridges and furrows
830 on moraine crests and in inter-moraine troughs.

831

832 **Figure 3.** Results of vertical (Z_{diff} ; m) differencing of the UAV-SfM and TLS datasets
833 acquired at the end of season 1, represented as the mean difference within 10 m^2
834 grid cells. 83% of the UAV-SfM data were found to be within $\pm 0.1\text{ m}$ of the equivalent
835 TLS data. Profiles A-C are displayed in Fig. 4.

836

837

838 **Figure 4.** Moraine surface elevation profiles, extracted from gridded (0.2 m^2) digital
839 elevation models of TLS- and SfM-derived topographic datasets. Profile locations are
840 shown in Figures 3 and 6. Profiles A and B bisect the main central moraine crest,
841 whilst profile C is located on moraine deposits at the back of the embayment. Inset
842 numbered boxes in profiles A and C show areas referred to in the text.

843

844 **Figure 5.** Vertical component of 3D topographic change (Z_{diff}) overlain on a UAV-
845 SfM-derived hill-shaded DEM of the Patriot Hills blue-ice moraine complex.
846 Topographic evolution was quantified using the Multiscale Model to Model Cloud
847 Comparison (M3C2) algorithm in CloudCompare software. **(a)** UAV-SfM
848 orthophotograph of the study site. Panels **(b)** to **(f)** cover specific differencing epochs
849 using a combination of TLS and SfM data (see panel headings). Dashed line in **(b)** to
850 **(f)** indicates locations of primary moraine ridge crest.

851

852 **Figure 6.** Change detection mapping for **(a)** intra-annual (season 1 start to season 1
853 end) and **(b)** annual (season 1 start to season 2) differencing epochs. Horizontal
854 difference vectors (XY_{diff}) are scaled by magnitude and oriented according to the
855 direction of change. The vertical component of 3D change (Z_{diff}) is shown in the

856 background. Transects A-C denote the location of moraine surface profiles displayed
857 in Fig. 4. Red dashes on both panels show approximate location of primary moraine
858 ridge crest.

859

860 **Table 1.** Terrestrial laser scanning and UAV-SfM survey dates and registration
861 errors. Within each season, individual scans were registered to a single static
862 position to produce a single, merged point cloud (scan-scan registration error). TLS
863 data from the end of season 1 and for season 2 were subsequently registered to TLS
864 data acquired at the start of season 1, producing a project-project registration error.
865 The UAV-SfM data (season 1 end) were registered to TLS data from the end of
866 season 1.

867

868 **Table 2.** Registration error propagation for specific differencing epochs. The
869 propagated error for each differencing epoch is calculated using Eq. 3. The 95%
870 level of detection, or detection threshold is calculated in M3C2 as the product of the
871 propagated error and a measure of local point cloud roughness (Lague et al., 2013).
872 The results of 3D differencing were filtered in CloudCompare so that only differences
873 largest than the most conservative (largest) $LoD_{95\%}$ (i.e. 0.103 m) were considered to
874 represent significant change.

875

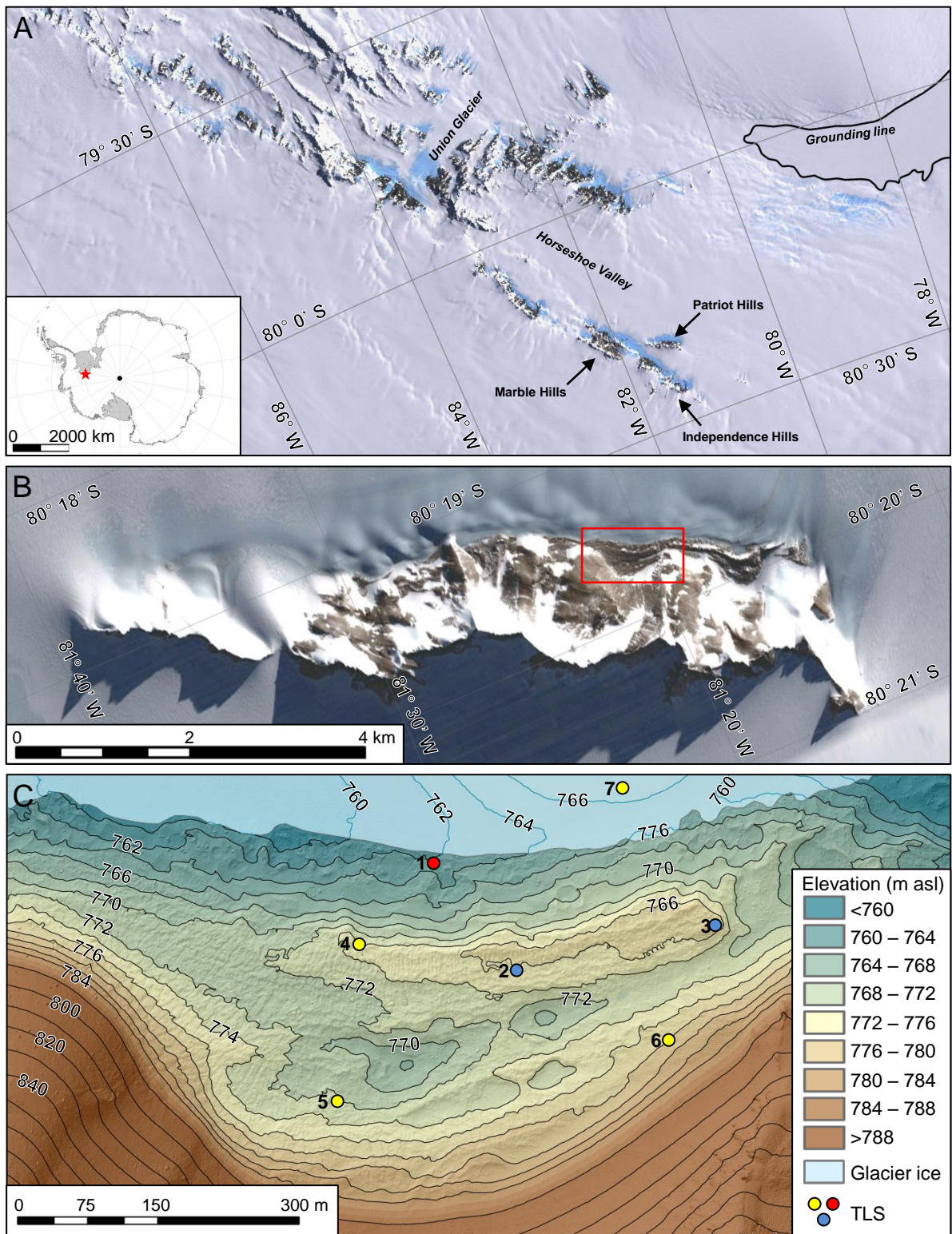


Figure 1. Blue-ice moraine embayment, Patriot Hills, Heritage Range, Antarctica. **(a)** Geographical context of Patriot Hills within the Heritage Range, southern Ellsworth Mountains. **(b)** The Patriot Hills massif. The location of the study embayment and area displayed in **(c)** highlighted in red. **(c)**: Detailed study site overview map. Contours and underlying hillshade are derived from a UAV-SfM-derived DEM. TLS positions for the start of season 1 are shown in red, blue and yellow. The two scan positions re-occupied at the end of season 1 are shown in blue, whilst the three scan positions reoccupied in season 2 are shown in blue and red. Background imagery: **(a)** © U.S. Geological Survey; **(b)** © 2015 DigitalGlobe, both extracted from Google Earth.

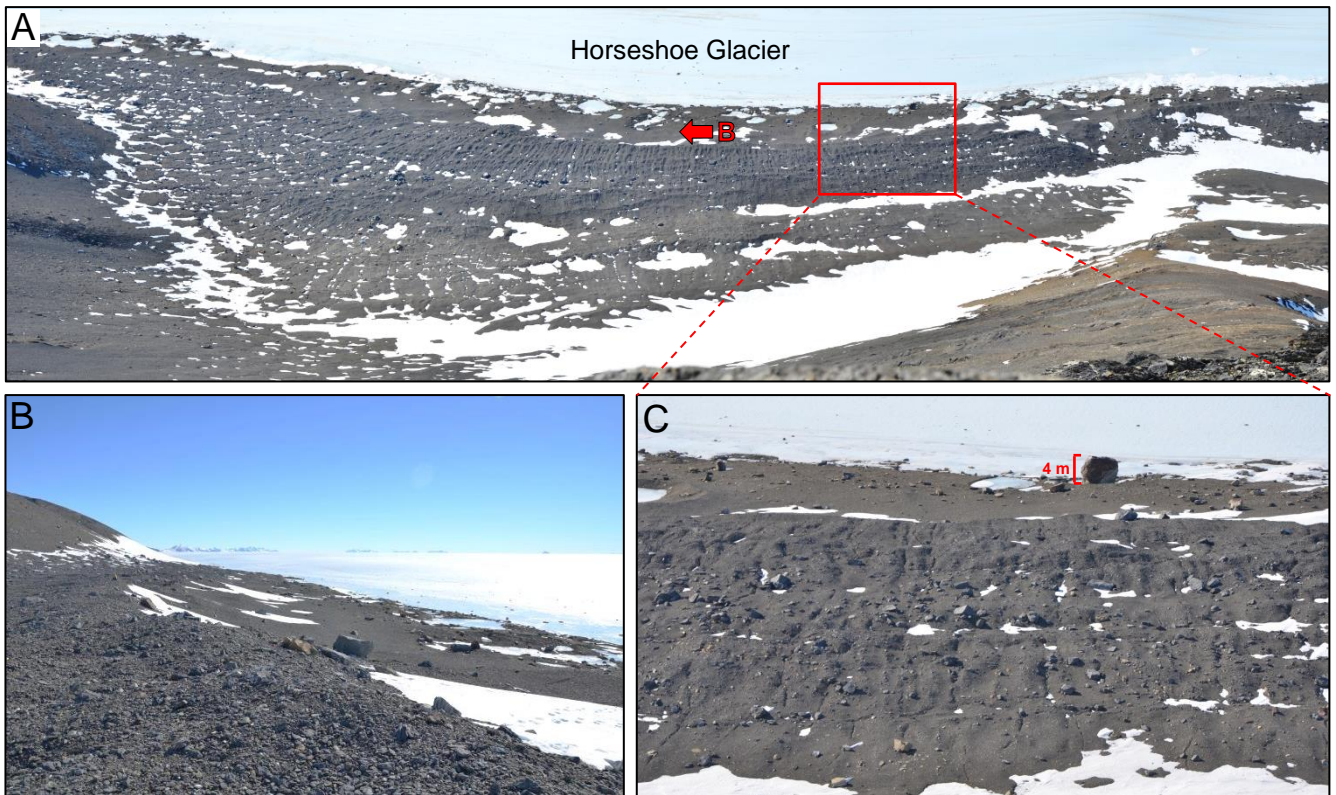


Figure 2. Field photographs of the Patriot Hills blue-ice moraine study site. **(a)** Panoramic photograph of the moraine embayment – view north-east towards the ice margin from the rear of the embayment. Area shown in **(c)** and position and view direction of camera **(b)** shown for reference. **(b)** View to the north-west with moraine crest in foreground and subdued, ice-marginal moraine surface topography in middle-ground. **(c)** Close-up of moraine topography, highlighting ridges and furrows on moraine crests and in inter-moraine troughs.

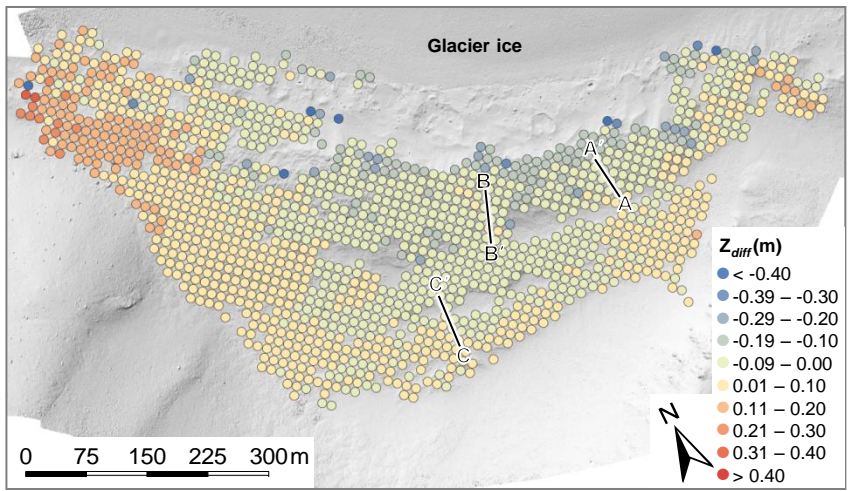


Figure 3. Results of vertical (Z_{diff} ; m) differencing of the UAV-SfM and TLS datasets acquired at the end of season 1, represented as the average difference within 10 m^2 grid cells. 83% of the UAV-SfM data were found to be within $\pm 0.1 \text{ m}$ of the equivalent TLS data. Profiles A-C are displayed in Fig. 4.

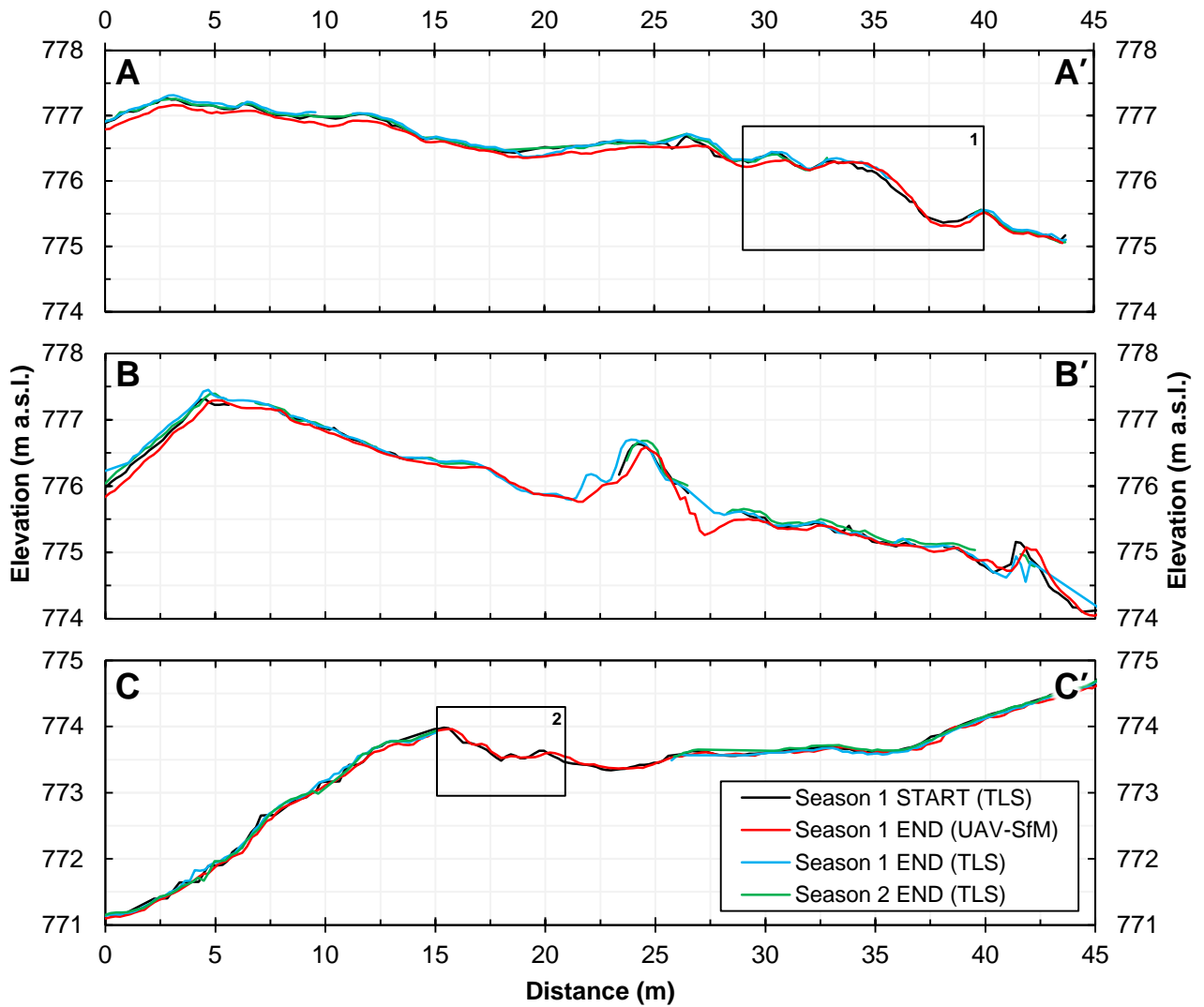


Figure 4. Moraine surface elevation profiles, extracted from gridded (0.2 m^2) digital elevation models of TLS- and SfM-derived topographic datasets. Profile locations are shown in Fig. 4. Profiles A and B bisect the main central moraine crest, whilst profile C is located on moraine deposits at the back of the embayment. Inset numbered boxes in profiles A and C show areas referred to in the text.

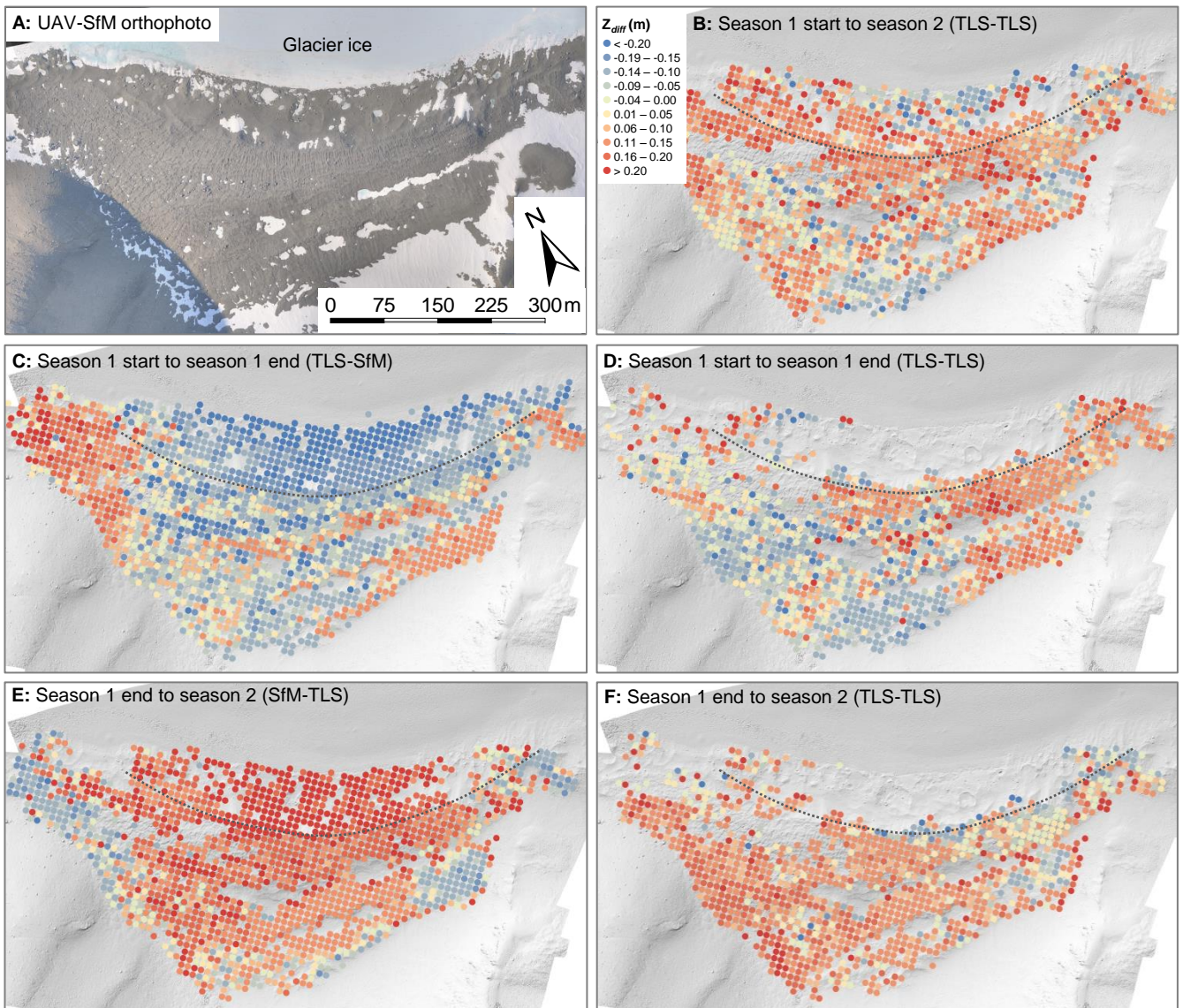


Figure 5. Vertical component of 3D topographic change (Z_{diff}) overlain on a UAV-SfM-derived hill-shaded DEM of the Patriot Hills blue-ice moraine complex. Topographic evolution was quantified using the Multiscale Model to Model Cloud Comparison (M3C2) algorithm in CloudCompare software. **(a)** UAV-SfM orthophoto of the study site. Panels **(b)** to **(f)** cover specific differencing epochs using a combination of TLS and SfM data (see panel headings). Dashed line in **(b)** to **(f)** indicates locations of primary moraine ridge crest.

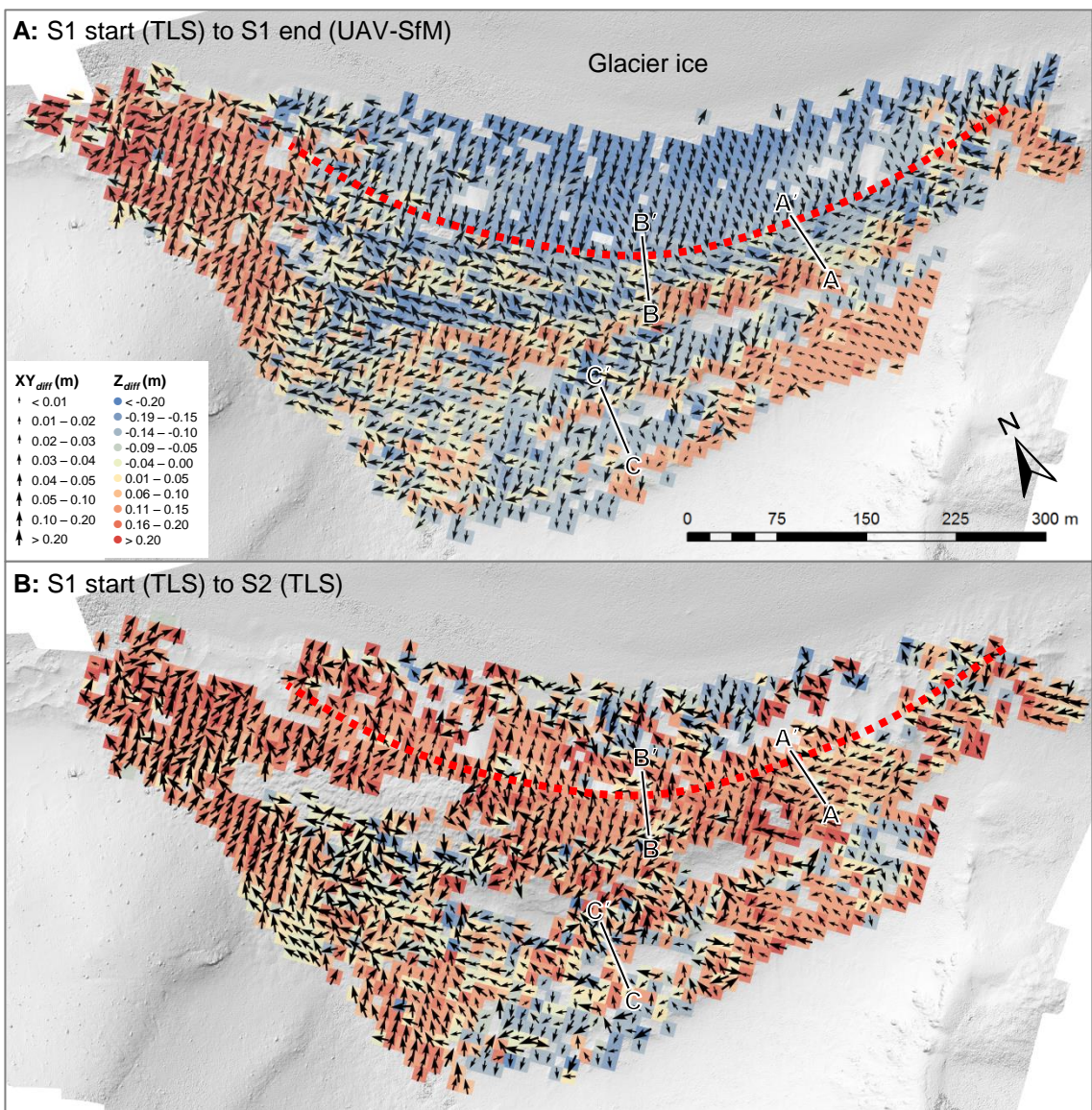


Figure 6. Change detection mapping for **(a)** intra-annual (season 1 start to season 1 end) and **(b)** annual (season 1 start to season 2) differencing epochs. Horizontal difference vectors (XY_{diff}) are scaled by magnitude and oriented according to the direction of change. The vertical component of 3D change (Z_{diff}) is shown in the background. Transects A-C denote the location of moraine surface profiles displayed in Fig. 5. Red dashes on both panels show approximate location of primary moraine ridge crest.